Contents lists available at ScienceDirect

Journal of Contaminant Hydrology

journal homepage: www.elsevier.com

Chromatographic analysis of the acidity-salinity transport system

Colin J. McNeece[a, *], Johannes Lützenkirchen[b], Marc A. Hesse[a, c]

[a] The University of Texas at Austin, Department of Geological Sciences, 2305 Speedway Stop C1160, Austin, TX 78712-1692, United States of America
[b] Karlsruher Institut für Technologie, Institut für Nukleare Entsorgung, Hermann-von-Helmholtz-Platz 1, Eggenstein-Leopoldshafen 76344, Germany
[c] The University of Texas at Austin, The Institute for Computational Engineering and Sciences, 201 E. 24th Street, Austin, Texas 78712, United States of America

ARTICLE INFO

Keywords:
Reactive transport
Chromatography
Electric double layer
Hyperbolic theory
Surface complexation
Triple layer model

ABSTRACT

The effects of acidity and salinity on solute transport in porous media are important to a diverse range of fields from seawater intrusion to nuclear waste storage. Recent transport experiments in quartz sand show the difficulty in capturing the coupling of acidity and salinity under acidic conditions for this system. Here we study the ability of different surface complexation models to capture this coupling, through an analysis of the reactive transport equations in the limit of no diffusion. This chromatographic analysis leads to a graphical representation of the full set of solutions in the phase plane, thus allowing a comprehensive comparison of the transport behavior arising from different SCMs. The analysis shows that the predicted coupling is improved by including amphoteric behavior of the quartz surface. The inclusion of a secondary proton sorption reaction increases the magnitude of surface charge under acidic conditions strengthening the acidity-salinity coupling. This suggests that even though the overall surface is negative above the point of zero charge, positively charged sites play an important role in the reactive transport of acidity and salinity.

1. Introduction

To first-order the surface charge and therefore chemical behavior of reactive media is determined by aqueous acidity and salinity. These variables are coupled through the effects of ionic strength on the activity of aqueous species, and the electrical properties of the diffuse layer, as well as competitive sorption of ions for surface sites (Meeussen et al., 1996). Much work has been done in the development of surface chemistry models which can mechanistically capture this behavior, so called surface complexation models (SCMs) (Sposito, 2004). Among the most advanced are the triple layer model (TLM) and the three plane model (TPM). These models have been used to successfully account for the acidity-salinity coupling of many oxide surfaces in batch settings. However, current chemical model conventions for the quartz surface cannot quantitatively capture the coupling in reactive transport systems (McNeece and Hesse, 2017). The error in predicted breakthrough curves is most noticeable in the acidic regime. Recent studies have shown that this failure is independent of parameterization, suggesting that the functional form of the surface chemistry model is inadequate. An understanding of the role of the surface chemistry model's formulation is therefore needed. Towards this effort we present a chromatographic analysis of the coupled acidity-salinity transport system under conditions appropriate for reactive transport experiments of McNeece and Hesse (2017).

Much scrutiny has been given to the surface behavior of quartz, yet controversy exists as to the nature and abundance of surface sites. Spectroscopic and titration experiments of quartz suggest that the surface is negatively charged over a large range of pH values (Ahmed, 1966; Anderson and Wickersheim, 1964; Bolt, 1957; Koretsky et al., 1997; Li and Bruyn, 1966; Morrow and Cody, 1976). Classic models of the quartz surface therefore consider a one-site formulation, such that the surface can be only negative or neutral via a single proton sorption reaction. However, it is fairly well established that the point of zero charge of the quartz surface is around pH 3 according to Kosmulski (2001), therefore a positive charge is possible and it is reasonable to consider two protonation reactions. In a minority of other studies a more complex behavior has been reported, suggesting a further proton reaction on a second site (Duval et al., 2002; Leung et al., 2009; Ong et al., 1992; Pokrovsky et al., 2006; Zoback, 2012). Clearly, controversy remains as to the proper formulation of the surface chemistry model of quartz. Here we explore the single site formulation through a parameter adjustment of the two-step model, and determine the role of surface reaction on transport behavior. This example will serve as a template

* Corresponding author.
Email addresses: cmcneece@utexas.edu (C.J. McNeece); johannes.luetzenkirchen@kit.edu (J. Lützenkirchen); mhesse@jsg.utexas.edu (M.A. Hesse)

https://doi.org/10.1016/j.jconhyd.2018.08.001
Received 22 February 2018; Received in revised form 29 June 2018; Accepted 7 August 2018
Available online xxx
0169-7722/

to encourage the further comparison of model formulation through chromatographic analysis.

The mathematical basis of multiple solute chromatography was developed for charged ions undergoing Langmuir type sorption and ion exchange (Charbeneau, 1981, 1988; Lake, 1989; Rhee et al., 1970; Temple, 1983). More recently chromatographic analysis was conducted on pH dependent sorption (Prigiobbe et al., 2012) and to the single component acidity system using SCMs (McNeece and Hesse, 2016; Meeussen et al., 1999; Scheidegger et al., 1994). Here we extend chromatographic theory to the coupled acidity-salinity transport system. The analysis allows a graphical representation of transport behavior as a function of injected and initial composition. This visual tool is known as the hodograph plane, and facilitates a direct comparison of the transport behavior for a given surface complexation model and the concomitant parameterization.

Below we introduce the reactive transport model, being composed of the surface chemistry model and conservation law. We then present the chromatographic analysis and hodograph plane. Finally, we use the hodograph plane to explore the role of surface chemistry model formulation on predicted transport behavior by a comparison to column experiments.

2. Reactive transport model

Here we introduce the chemical model of the coupled acidity-salinity system in quartz sand and show the resulting sorption isotherms. We then introduce the transport equations of the conserved quantities.

2.1. Surface complexation model

In order to capture the acidity-salinity coupling in reactive media, both aqueous and surface speciation must be considered. In the simple system, the auto-ionization of water is the most relevant aqueous reaction

$$H_2O \leftrightarrow H^+ + OH^-. \tag{1}$$

The surface speciation is characterized by the sorption of protons, sodium, and chloride. Below are the reactions and their associated equilibrium constants,

$$\equiv SiO^- + H^+ \leftrightarrow \equiv SiOH, \qquad K_{H,1}, \tag{2}$$

$$\equiv SiOH + H^+ \leftrightarrow \equiv SiOH_2^+, \qquad K_{H,2}, \tag{3}$$

$$\equiv SiO^- + Na^+ \leftrightarrow \equiv SiO^- - Na^+, \qquad K_{Na}, \tag{4}$$

$$\equiv SiOH_2^+ + Cl^- \leftrightarrow \equiv SiOH_2^+ - Cl^-, \qquad K_{Cl}, \tag{5}$$

where $\equiv$ denotes the quartz mineral structure. The quartz surface has a point of zero charge near pH = 3 (Kosmulski, 2001). Therefore, in the literature it is often assumed that reactions (3) and (5) are negligible at higher pH values and are dropped. For the mathematical analysis we will adopt this convention. In the discussion section, this assumption will be relaxed in order to explore the role of these reactions on the mathematical solution structure.

To determine the equilibrium distribution of the above species, the chemical reactions are coupled to a given SCM. These models attempt to account for the contribution of electrostatic interactions at the mineral surface in determining the reactivity of surface sites. Among the most robust of these models is the triple layer model (TLM). Westall and Hohl (1980) offer a comprehensive summary of this model and others.

The TPM approximates the mineral-water interface by three capacitors in series, including the diffuse layer. The inner layer capacitors are segmented by planes of charge accumulation. The mineral surface charge is determined by the sorption of small ions (i.e. H^+ and OH^-) which sorb directly to the surface sites. Such sorption reactions are known as inner-sphere surface complexes. In the case of protons the size is not such that a charge distribution is required. Larger ions such as sodium typically retain their solvation shell. The volume of solvation waters geometrically inhibits direct binding to a surface site and limits the uptake to a discrete distance from the plane of the surface sites. Therefore, such ions are considered to sorb at a distance of roughly the size of a water molecule plus the radius of the bare ion (i.e. the radius of the hydrated ion) from the mineral surface and are called outer-sphere surface complexes. This plane of adsorption is known as the inner Helmholtz plane (IHP). Because of the distance separating the mineral surface and the sorbed species, outer-sphere complexes when treated as point charges contribute their charge to the IHP. At some distance beyond the IHP a diffuse ion cloud balances the cumulative charge of the mineral surface and IHP. This plane is known as the outer Helmholtz plane (OHP). The region between the mineral surface and the OHP is known as the Stern layer. The region beyond the OHP is known as the diffuse layer.

The charge of the mineral surface and IHP are mathematically defined as linear combinations of the charged species residing on each plane

$$\sigma_0 = \Sigma SiO \frac{F}{Sa}\left(-[\equiv SiO^-] - \left[\equiv SiO^- - Na^+\right]\right), \tag{6}$$

$$\sigma_1 = \Sigma SiO \frac{F}{Sa}\left(\left[\equiv SiO^- - Na^+\right]\right), \tag{7}$$

where σ_0 and σ_1 are the surface charge densities of the mineral surface and IHP respectively (C/m^2), F is Faraday's constant (C/mol), S is the specific surface area of the material (m^2/kg), and a is the slurry density (kg/L). Quantities in brackets, [], when representing an aqueous species, give the molar concentration (M). When representing surface species, bracketed quantities give mole fraction, following the convention of Sverjensky (2005).

The inner and outer Stern layers are modeled as capacitors with constant capacitance density. The theoretical value of the capacitance density depends on surface geometry, and the temperature of the system. The diffuse layer is considered to have a variable capacitance density as determined by properties of the bulk fluid such as ionic strength, and temperature as well as surface geometry. These variables also influence the permittivity of the diffuse layer. The charge-potential relationships of these three layers within the TLM for a 1:1 background electrolyte are

$$\sigma_0 = C_1\left(\Psi_0 - \Psi_1\right), \tag{8}$$

$$\sigma_2 = -C_2\left(\Psi_1 - \Psi_2\right), \tag{9}$$

$$\sigma_2 = -\sqrt{8 \cdot 10^3 RTIe_o e_w}\ \sinh\left(\frac{F\Psi_2}{2RT}\right), \tag{10}$$

$$0 = \sigma_o + \sigma_1 + \sigma_2, \tag{11}$$

where σ_2 is the charge density of the OHP (C/m^2), C_1, and C_2 are the capacitance densities of the region between the mineral surface and IHP and stern layer respectively (F/m^2). Ψ_0, Ψ_1, and Ψ_2 are the electric potentials of the mineral surface, IHP, and OHP respectively (V), R is the gas constant (J/(K mol)), T is temperature (K), I is ionic strength (M), e_o is the permittivity of free space (F/m), and e_w is the dielectric constant of water (-). The Grahame equation, Eq. (10), is the integral of all charge within the diffuse layer. For non-symmetrical electrolyte solutions a more complex form of Eq. (10) is needed (Sposito, 2004). Additionally, Eq. (10) breaks down in systems with significant overlap of the diffuse layer. In a previous work we have demonstrated that this is not the case for the material studied here (McNeece and Hesse, 2017).

The present use of Eq. (10) is appropriate only for symmetrical 1:1 electrolyte solutions (Lutzenkirchen et al., 2015).

At local chemical equilibrium the electrostatic model is coupled to the chemical speciation through the laws of mass action

$$K_w = \{H^+\}\{OH^-\}, \tag{12}$$

$$K_{H,1} = \frac{[\equiv SiOH]}{[\equiv SiO^-]\{H^+\}\exp\left(\frac{-F\Psi_0}{RT}\right)}, \tag{13}$$

$$K_{Na} = \frac{\left[\equiv SiO^- - Na^+\right]\exp\left(\frac{F(\Psi_1-\Psi_0)}{RT}\right)}{[\equiv SiO^-]\{Na^+\}\exp\left(\frac{-F\Psi_0}{RT}\right)}, \tag{14}$$

where the quantities in braces, {}, are activities (-), being the product of the solute molar concentration, activity coefficient, and the inverse of the standard state for solutes (1 M) (White, 2013). In the range of ionic strengths considered here, the activity coefficients are well approximated by the extended Davies equation (Davies, 1962).

In the transport model it is convenient to consider the aqueous and surface concentrations of species separately, as their transport behavior differs, namely, sorbed species are considered to be immobile, and aqueous species move with the fluid. Therefore we introduce the variables

$$\mathbf{c} = \begin{Bmatrix} [Na^+] \\ [H^+] - [OH^-] \end{Bmatrix} = \begin{Bmatrix} c_{Na} \\ c_H \end{Bmatrix} \tag{15}$$

$$\mathbf{s} = \begin{Bmatrix} \Sigma SiO[\equiv SiO^- – Na^+] \\ \Sigma SiO[\equiv SiOH] \end{Bmatrix} = \begin{Bmatrix} s_{Na} \\ s_H \end{Bmatrix} \tag{16}$$

where **c** and **s** are the vectors of total aqueous and surface concentrations respectively.

The relationship between the total aqueous and sorbed concentrations determines transport behavior (McNeece and Hesse, 2016). Representative sorption isotherms are shown in Fig. 1. Parameter values are presented in Table 1. Values of $K_{H,1}$, K_{Na}, C_1, and C_2 are taken from Hiemstra et al. (1989). The approach involves the MUSIC model to

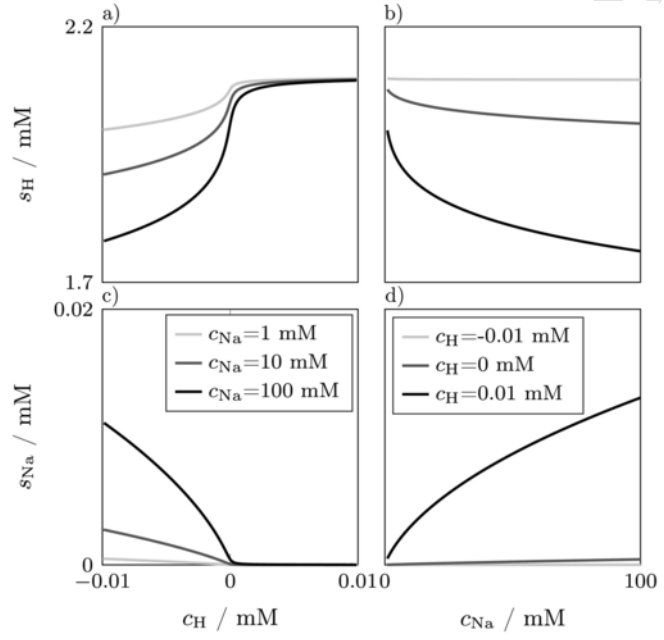

Fig. 1. Sorption isotherms. The sorbed concentration of a,b) protons and c,d) sodium as a function of aqueous concentrations.

Table 1
Parameterization. Reactive transport model parameter values for a column packed with quartz sand.

Parameter	Description	Value	Units
A	Column cross-sectional area	$1.7\cdot 10^{-4}$	m^2
a	Column slurry density	$5.5\cdot 10^{3}$	g/L
C_1	Capacitance density	3.3	F/m^2
C_2	Capacitance density	10^3	F/m^2
ϕ	Column porosity	0.325	-
K_{Na}	Reaction (4) eq. constant	$10^{-1.9}$	-
$K_{H,1}$	Reaction (2) eq. constant	$10^{7.5}$	-
K_w	Reaction (1) eq. constant	10^{-14}	-
L	Column length	0.37	m
q	Volumetric flow rate	$2\cdot 10^{-6}$	m^3/min
ρ_s	Surface site density	$4.6\cdot 10^{18}$	sites/m^2
S	Specific surface area	$5\cdot 10^{-2}$	m^2/g
T	Temperature	293	Kelvin

mechanistically determine the equilibrium constant $K_{H,1}$ and optimizes the other parameters by minimizing the error between the model and batch titration data produced by Bolt (1957). This model parameterization will be referred to as the "reference model." Notably in the reference model the value of the second capacitor is very high, which reduces a TLM or TPM to a basic Stern version of the interface.

It can be seen from Fig. 1 that the sorption isotherms show typical competitive sorption behavior in that the sorbed concentration of an element increases with aqueous concentration, while decreasing with an increase in competing ions. The inflection point in both s_H and s_{Na} is characteristic of pH dependent sorption processes and has interesting implications for transport behavior as will be discussed below.

2.2. Conservation laws

Here we consider the 1D reaction-advection-diffusion equation for the conserved quantities of acidity and salinity at local chemical equilibrium,

$$\left(\mathbf{I} + \nabla_{\mathbf{c}}\mathbf{s}(\mathbf{c})\right)\mathbf{c}_\tau + \mathbf{c}_z - \mathbf{Pe}^{-1}\mathbf{c}_{zz} = 0, \tag{17}$$

where **I** is the identity matrix, $z = x/L$, and $\tau = qt/(\phi AL)$ are dimensionless space and time respectively, and $\mathbf{P}\,\mathbf{e} = qL/(\phi A\,\mathbf{D})$ is the Péclet number where q is the volumetric flow rate, A is the column cross-sectional area, L is the column length, and **D** is the hydrodynamic dispersion tensor for each component (Appelo and Postma, 2005). The dimensionless time, $\tau = 1$, is equivalent to the time required for the injection of one pore volume. In Eq. (17) the Jacobian of the sorption isotherm with respect to the aqueous concentration is given by

$$\nabla_{\mathbf{c}}\mathbf{s}(\mathbf{c}) = \begin{Bmatrix} \frac{\partial s_{Na}}{\partial c_{Na}} & \frac{\partial s_{Na}}{\partial c_H} \\ \frac{\partial s_H}{\partial c_{Na}} & \frac{\partial s_H}{\partial c_H} \end{Bmatrix}. \tag{18}$$

In the column experiments of interest, the inferred Péclet numbers are $\mathcal{O}(10^3)$ (McNeece and Hesse, 2016), thus we consider the hyperbolic limit of Eq. (17), $\mathbf{P}\,\mathbf{e} \to \infty$,

$$\left(\mathbf{I} + \nabla_{\mathbf{c}}\mathbf{s}(\mathbf{c})\right)\mathbf{c}_\tau + \mathbf{c}_z = 0. \tag{19}$$

A typical column flood experiment procedure can be represented as a Riemann problem, with a piece-wise constant initial condition having a step about the origin,

$$\mathbf{c}(z, \tau = 0) = \begin{cases} \mathbf{c}_{inj} & z<0, \\ \mathbf{c}_{ini} & z \geq 0. \end{cases} \tag{20}$$

where $\mathbf{c}_{ini}$ and $\mathbf{c}_{inj}$ are the initial and injected concentrations respectively.

3. Solution by method of characteristics

Here we detail the procedure for the semi-analytic solution of the reactive transport model using the theory of hyperbolic conservation laws which is the equivalent to the theory of chromatography for reactive transport.

We are interested in predicting experimental effluent histories. In reactive transport problems the effluent history is typically observed, and the nonlinearity occurs in the accumulation term. It is therefore natural to follow the chromatographic convention and describe the solution in terms of retardation rather than velocity (Rhee et al., 2001a,b).

3.1. Eigenvalue problem

The form of the reactive transport model, Eq. (19), and the initial condition, Eq. (20), allows the introduction of the retardation as the similarity variable

$$\eta := \tau/z. \tag{21}$$

Substitution of η into Eq. (19) reduces the system of partial differential equations to ordinary differential equations in the form of an eigenvalue problem

$$\left(\mathbf{I} + \nabla_{\mathbf{c}}\mathbf{s}(\mathbf{c}) - \theta_p(\mathbf{c})\right)\mathbf{r}_p = 0, \tag{22}$$

where $\theta_p(\mathbf{c}) = \eta = \tau/z$ are the eigenvalues and

$$\mathbf{r}_p(\mathbf{c}) = \left(\frac{\mathrm{d}\mathbf{c}}{\mathrm{d}\eta}\right)_p \tag{23}$$

are the eigenvectors.

Here we consider a 2×2 system of coupled equations for the transport of acidity and salinity, resulting in two sets of eigenvalues and eigenvectors, $p \in [1, 2]$. Below we demonstrate, computationally, that the eigenvalues are real and distinct, $0 < \theta_1 < \theta_2$, so that the system of equations is strictly hyperbolic (LeVeque, 1992). This results in a front structure composed of two waves, $\mathscr{W}_1$ and $\mathscr{W}_2$, connecting the initial, $\mathbf{c}_{\mathrm{ini}}$, and injected state, $\mathbf{c}_{\mathrm{inj}}$. These waves are joined at an intermediate state, $\mathbf{c}_{\mathrm{int}}$, and are ordered from the fastest to the slowest

$$\mathbf{c}_{\mathrm{ini}} \xrightarrow{\mathscr{W}_1} \mathbf{c}_{\mathrm{int}} \xrightarrow{\mathscr{W}_2} \mathbf{c}_{\mathrm{inj}}. \tag{24}$$

The solution of the transport problem requires the determination of the intermediate state $\mathbf{c}_{\mathrm{int}}$ and the wave structures $\mathscr{W}_1$ and $\mathscr{W}_2$. The eigenvectors give the composition variation along these waves, while eigenvalues give the retardation of their arrival time. We will see that there are four possible wave structures: a smooth variation in composition known as a rarefaction, $\mathscr{R}$; a sharp variation known as a shock, $\mathscr{S}$; and two composite waves which contain both a smooth and a discontinuous change in concentration, $\mathscr{R}\mathscr{S}$ and $\mathscr{S}\mathscr{R}$, known as rarefaction-shocks and shock-rarefactions respectively. Here the symbol ordering corresponds to segment arrival order.

3.2. Eigenvalues and retardations

A closed form solution to the eigenvalue problem is intractable, because local chemical equilibrium involves the complex set of nonlinear equations (Eqs (6)–(16)). Therefore Eq. (22) is solved numerically and the two eigenvalues are plotted in Fig. 2. Here a smaller eigenvalue is equivalent to a faster travel speed/lower retardation. The smallest eigenvalue, θ_1, is approximately unity and is related to the breakthrough of the salinity front. In contrast, θ_2 is a strong function of both the acidity and salinity, with a local maximum near neutral acidity.

Fig. 2 shows that over the composition space investigated here, $1 \leq \theta_1 < \theta_2$. This implies that the first wave never arrives before a tracer

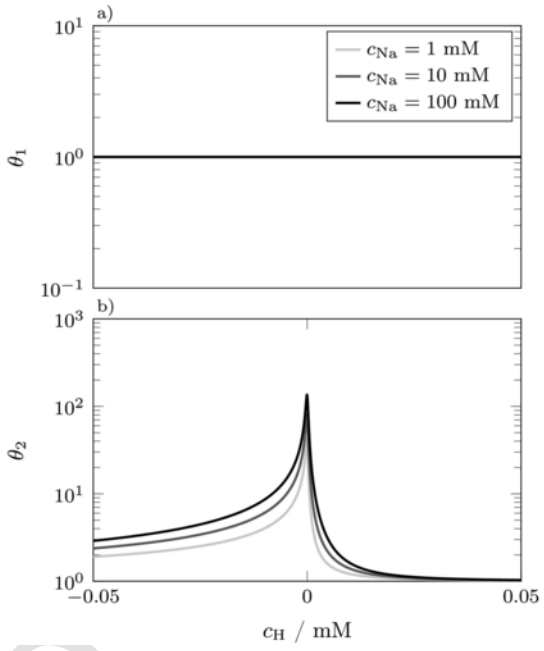

Fig. 2. Eigenvalues. The eigenvalues of the coupled acidity-salinity system. Eigenvalues correspond to retardation. There is strong coupling between $\mathbf{c}$ and θ_2 whereas θ_1 remains unchanged.

breaks through, and that the second wave is always delayed such that an intermediate state exists.

From a previous analysis it is clear that the magnitude of the eigenvalue θ_2 is directly proportional to the derivative of the isotherm in Fig. 1a (McNeece and Hesse, 2016, 2017; Prigiobbe et al., 2013; Scheidegger et al., 1994). An inflection point in the sorption isotherm, is typical of the proton sorption system (Prigiobbe et al., 2012) and leads to the local maximum in θ_2 that is observed in Fig. 2b. Hence, the hyperbolic system is non-genuinely non-linear (LeVeque, 1992) and allows the formation of composite waves. The implications of the inflection point for transport will be considered below and have been discussed for a system with constant salinity (McNeece and Hesse, 2016; Meeussen et al., 1999; Scheidegger et al., 1994).

3.3. Eigenvectors and composition pathways

Eigenvectors give the variation of composition along the waves which compose the solution structure. An integration of the eigenvectors gives the composition paths, also known as integral curves, $\mathbf{\Gamma}_p$,

$$\mathbf{\Gamma}_p = \mathbf{c}_o + \int_0^{\eta} \mathbf{r}_p(\mathbf{c})\mathrm{d}\eta'. \tag{25}$$

where $\mathbf{c}_o$ is a starting point in composition space. The reactive transport model is a 2×2 system, thus there are two sets of composition paths, which are shown in Fig. 3. All rarefaction waves, $\mathscr{R}_p$, lie along these composition paths. Plots of the dependent variables, c_{H} and c_{Na}, are referred to as phase or hodograph planes in the context of hyperbolic conservation laws (LeVeque, 1992). In chromatography and reactive transport Fig. 3 is called composition space (Rhee et al., 2001b).

3.4. Shocks and Hugoniot loci

Shocks form in the hyperbolic limit when the displacing composition has a lower retardation, θ_p, than the composition being displaced. This results in a triple-valued problem which is replaced by a mass conserving shock according to the Rankine-Hugoniot jump condition

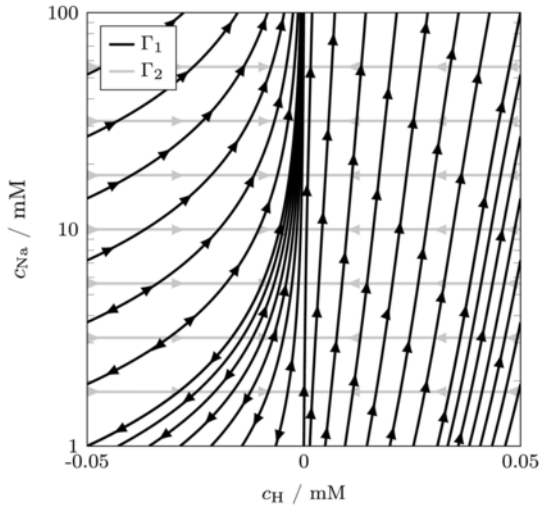

Fig. 3. Composition paths. The hodograph plane of the acidity-salinity transport system. Arrows show the direction of increasing eigenvalues along each composition path.

$$\widetilde{\theta}_p(\mathbf{c}^+, \mathbf{c}^-) = 1 + \frac{\mathbf{s}(\mathbf{c}^+) - \mathbf{s}(\mathbf{c}^-)}{\mathbf{c}^+ - \mathbf{c}^-}, \tag{26}$$

where $\widetilde{\theta}_p(\mathbf{c}^+, \mathbf{c}^-)$ is the retardation of the shock, and superscripts + and − correspond to the composition on either side of the jump (Rhee et al., 2001a,b). In the case where diffusive terms are also considered such waves will widen until an equilibrium width is achieved, the width being determined by the hydrodynamic dispersion (Rhee et al., 1971).

The right hand side of Eq. (26) can be rewritten as the following non-linear scalar algebraic equation

$$\frac{s_H^+ - s_H^-}{c_H^+ - c_H^-} - \frac{s_{Na}^+ - s_{Na}^-}{c_{Na}^+ - c_{Na}^-} = 0. \tag{27}$$

Given either $\mathbf{c}^+$ or $\mathbf{c}^-$ and solving for the other gives the locus of points that satisfy the conditions for a mass conserving shock, known as the Hugoniot loci, $\mathscr{H}_p$. The form of Eq. (27) makes clear that the discontinuity in each composition arrives with the same retardation, $\widetilde{\theta}_p$. The Hugoniot loci for several points are shown in Fig. 4. The Hugoniot loci must be tangent to the composition paths at the point under consideration. In the system considered, the Hugoniot loci are approximately coincident with the composition paths throughout the hodograph plane, and therefore only the integral curves are shown in the subsequent hodograph planes. However, in systems with highly curved composition paths, integral curves and Hugoniot loci often deviate (Johansen et al., 2005; LeVeque, 1992; Prigiobbe et al., 2013).

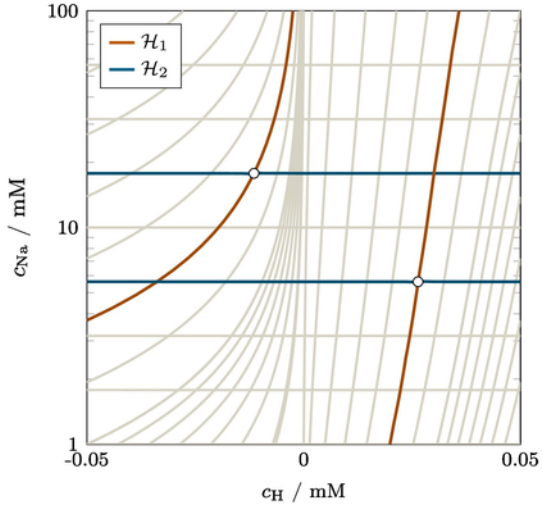

Fig. 4. Hugoniot loci. The set of Hugoniot loci for two points in the acidity-salinity system. The loci are nearly coincident to composition paths throughout composition space.

3.5. Composite waves and inflection loci

The sorption isotherms shown in Fig. 1a and d have inflection points near neutral pH, $c_H = 0$. This is due to the aqueous reaction (1) and marks the transition from $c_H \approx [H^+]$ to $c_H \approx -[OH^-]$ (McNeece and Hesse, 2016). This leads to the local maximum observed in θ_2 as seen in Fig. 2b. Equivalent inflection loci, $\mathscr{I}_p$, can be defined in the two-component system as follows

$$\nabla\theta_p \cdot \mathbf{r}_p(\mathbf{c}) = 0, \tag{28}$$

and are shown in Fig. 5.

The inflection loci $\mathscr{I}_1$ and $\mathscr{I}_2$ along $c_H \approx 0$ are nearly coincident and mark a local maximum in both θ_1 and θ_2. A second branch of $\mathscr{I}_1$ in the basic regime marks a small local minimum in θ_1 which is replotted in more detail in Fig. 6.

A wave $\mathscr{W}_p$ can be composite, if the composition path crosses $\mathscr{I}_p$. If the solution involves a composite wave, an additional concentration, corresponding to the transition in wave type, must be determined. This composition, $\mathbf{c}^*$, is found by equating the eigenvalue, $\theta_p(\mathbf{c}^*)$, along the rarefaction, with the retardation of the connecting shock given by,

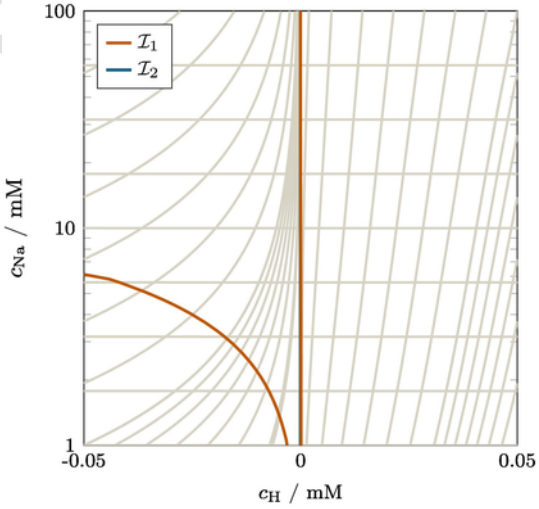

Fig. 5. Inflection loci. The inflection loci are plotted here overlaying the hodograph plane.

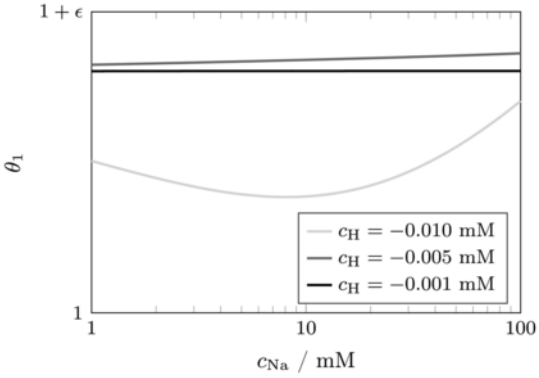

Fig. 6. Fast-wave eigenvalues. The fast wave eigenvalues are plotted for several constant acidity values in the basic regime showing the local minimum in θ_1. $\epsilon = 2 \cdot 10^{-6}$.

$$\widetilde{\theta}_p(\mathbf{c}^*) = 1 + \frac{\mathbf{s}(\mathbf{c}^*) - \mathbf{s}(\mathbf{c}^-)}{\mathbf{c}^* - \mathbf{c}^-}, \tag{29}$$

where $\mathbf{c}^-$ is the composition connected to $\mathbf{c}$ * across the shock. In problems with a single component, this construction is equivalent to finding the cord that is tangent to the sorption isotherm (McNeece and Hesse, 2016; Scheidegger et al., 1994).

3.6. Solution construction

Because integral curves and Hugoniot loci coincide, the hodograph plane is independent of initial and injected composition, and therefore gives a universal representation of the solution structure. This allows a determination of the transport solution by visual inspection of the hodograph plane. Such a construction and the accompanying breakthrough curves are illustrated in Fig. 7 for two particular compositions. For clarity, we first consider examples without composite waves, whose construction will be discussed afterwards.

The solution construction proceeds by tracing $\mathbf{\Gamma}_1$ from $\mathbf{c}_{\text{ini}}$ and $\mathbf{\Gamma}_2$ from $\mathbf{c}_{\text{inj}}$. The composition $\mathbf{c}_{\text{int}}$ is given by the point where $\mathbf{\Gamma}_1$ and $\mathbf{\Gamma}_2$ intersect. At the intermediate state the composition path of the solution switches from $\mathbf{\Gamma}_1$ to $\mathbf{\Gamma}_2$.

The structure of the wave $\mathscr{W}_p$ is determined by the evolution of θ_p along $\mathbf{\Gamma}_p$. In particular, if θ_1 decreases along $\mathbf{\Gamma}_1$ from $\mathbf{c}_{\text{ini}}$ to $\mathbf{c}_{\text{int}}$ then $\mathscr{W}_1$ is a rarefaction, otherwise it is a shock. Similarly, if θ_2 decreases along $\mathbf{\Gamma}_2$ from $\mathbf{c}_{\text{int}}$ to $\mathbf{c}_{\text{inj}}$ then $\mathscr{W}_2$ is a rarefaction. The direction of increasing θ_p is shown by arrows along Γ_p. Therefore, for the particular $\mathbf{c}_{\text{ini}}$ and $\mathbf{c}_{\text{inj}}$ chosen in Fig. 7a, the solution structure is

$$\mathbf{c}_{\text{ini}} \xrightarrow{\mathscr{S}_1} \mathbf{c}_{\text{int}} \xrightarrow{\mathscr{R}_2} \mathbf{c}_{\text{inj}}. \tag{30}$$

Fig. 7b and c shows the corresponding effluent profiles. The coupling of acidity to salinity leads to a significant reduction of the acidity at the intermediate state. After some time, the acidity gradually increases to $\mathbf{c}_{\text{inj}}$ as the second wave elutes. Note that the salinity remains constant along the second wave, because salinity does not change along $\mathbf{\Gamma}_2$.

In Fig. 7d we consider the case where $\mathbf{c}_{\text{ini}}$ and $\mathbf{c}_{\text{inj}}$ are switched. From the geometry of the hodograph plane, it is clear that the morphology of the waves is reversed and the intermediate state requires an increase in acidity. The variation in θ_1 along $\mathbf{\Gamma}_1$ is negligible, hence the rarefaction becomes very steep and is indistinguishable from a shock. Therefore, the first wave arrives without retardation and is followed by a persistent intermediate state at a higher acidity. The second wave is a shock, with no change in salinity.

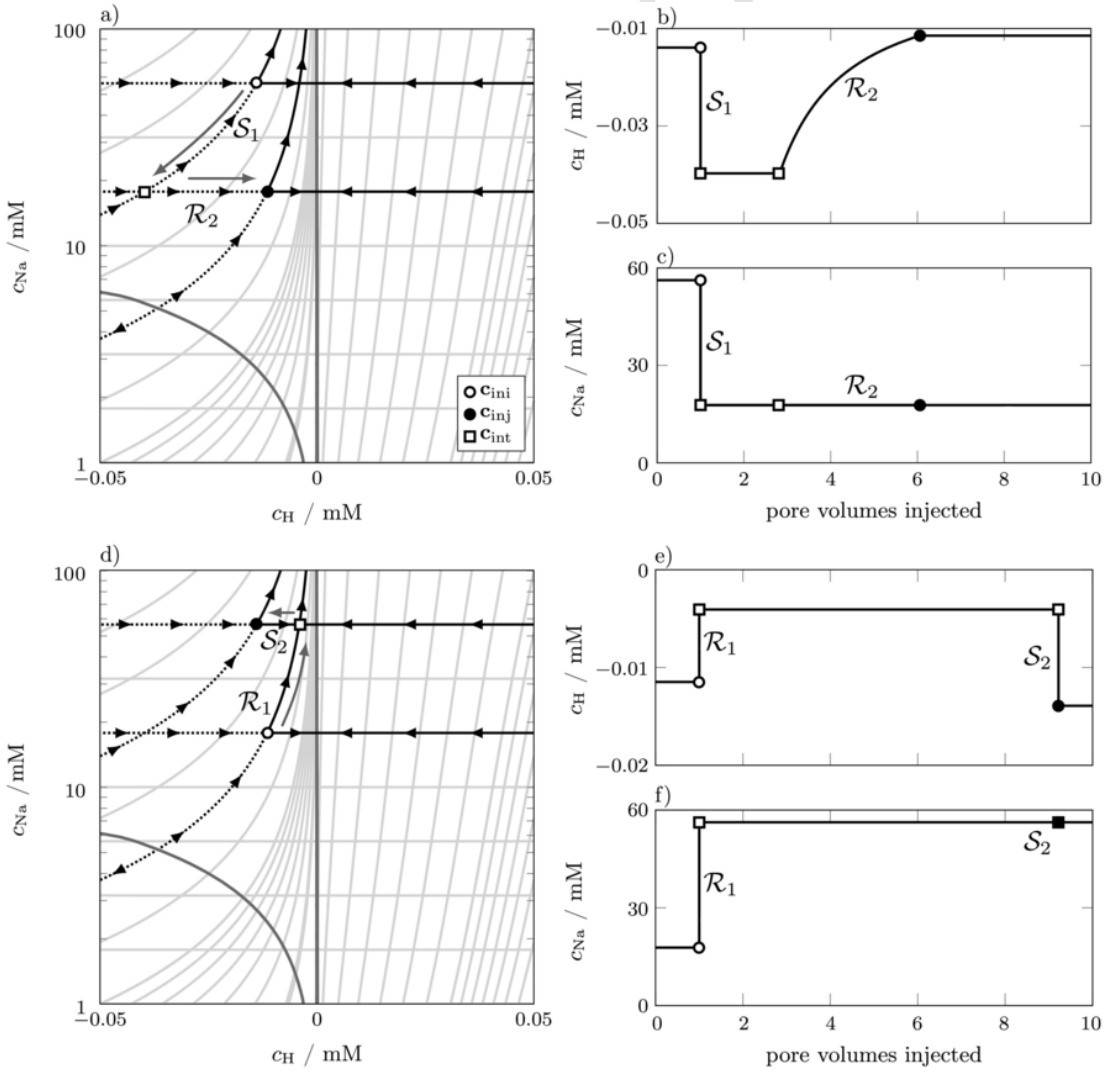

Fig. 7. Construction of solution. The solution structure for two different initial conditions plotted and on a,d) the hodograph plane and the resulting elution curves for b,e) acidity and c,f) salinity.

Next we consider two cases which lead to the formation of composite waves. First we consider the case of a composite wave during a constant salinity experiment, as has been discussed by McNeece and Hesse (2016), shown in burnt orange in Fig. 8. Here the initial and injected condition lie on the same $\mathbf{\Gamma}_2$ so that there is no intermediate state and the solution is comprised of a single wave. In this case, a composite wave forms as $\mathbf{c}_{\text{ini}}$ and $\mathbf{c}_{\text{inj}}$ straddle the inflection loci $\mathscr{I}_2$ along $\mathbf{\Gamma}_2$. The effluent profile shown in Fig. 8 b illustrates the morphological transition of $\mathscr{W}_2$ from a rarefaction to a shock at $\mathbf{c}^*$. Unlike a concatenation of simple waves, in composite waves a shock and rarefaction are not separated by an intermediate state. This composite wave structure has been observed experimentally and is a distinct feature of proton transport (McNeece and Hesse, 2017; Meeussen et al., 1999; Scheidegger et al., 1993).

Strictly, a composite path also exits along $\mathbf{\Gamma}_1$ in the blue example of Fig. 8 as $\mathscr{W}_1$ crosses $\mathscr{I}_1$. However, due to the near constant eigenvalue, the composite wave is visually indistinguishable from a discontinuity.

3.7. Interpretation of the hodograph plane

The hodograph plane shows that the acidity-salinity coupling is one-way, i.e. changes in salinity affect acidity, and not vice versa; as much is evident from the eigenvalues as plotted in Fig. 2. The curved, near vertical shape of $\mathbf{\Gamma}_1$ implies that any change in injected salinity, is accompanied by a change in acidity. In contrast, $\mathbf{\Gamma}_2$ is horizontal, so that changes in injected acidity do not affect salinity. Therefore, the best measure of the acidity-salinity coupling is the magnitude of displacement in acidity across the first wave, $\mathscr{W}_1$, which is measured by the intermediate state, $\mathbf{c}_{\text{int}}$. We will therefore refer to the first wave as the salinity wave, and the second as the acidity wave.

In addition, the hodograph plane implies the following set of general behaviors for the acidity-salinity system:

- An increase in salinity leads to an increase in acidity, because the slope of $\mathbf{\Gamma}_1$ is positive across composition space.
- The larger the change in salinity, the larger the change in acidity.
- The acidity-salinity coupling never changes the sign of the acidity, i.e., a basic solution cannot become acidic and vice versa, across the salinity wave. This is due to $\mathbf{\Gamma}_1$ never crossing $c_{\text{H}} = 0$.

The hodograph plane may then be used to design targeted experimental efforts. As stated previously, there is negligible coupling of acidity and salinity transport along $\mathbf{\Gamma}_2$. Therefore, column experiments where salinity is held constant, and pH is varied, can inform the transport behavior of acidity directly, but do not inform acidity-salinity coupling (McNeece and Hesse, 2016). Similarly, the hodograph plane shows that curvature of $\mathbf{\Gamma}_1$ is the distinguishing characteristic of the acidity-salinity coupling. McNeece and Hesse (2017) used this observation to design a suit of column experiments which explore the acidity-salinity coupling by holding acidity constant while varying injected salinity.

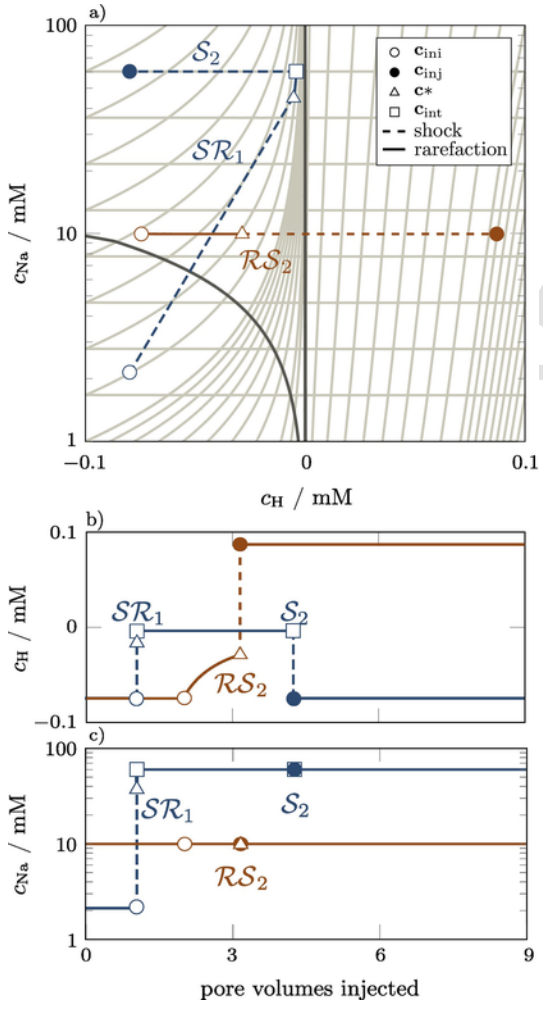

Fig. 8. Composite waves. The solution construction of two composite wave examples is shown. Dashed lines show shock waves, while solid lines show rarefactions. The fast wave of the orange example is a wave with no change in composition.

4. Transport experiments

In this work we compare the analytic transport predictions to transport experiments presented in McNeece and Hesse (2017). Here we briefly summarize the surface characterization efforts and column flood experiment procedure of the aforementioned manuscript.

4.1. Surface characterization

Column experiments were performed through Jurassic age beach sand composed of 99.9% quartz as confirmed by visual inspection in thin section and energy dispersivity spectroscopy. The average grain size was $1.2 \cdot 10^{-4}$ m as reported by the vendor. The specific surface area, S, as determined by Brunauer-Emmett-Teller (BET) surface area analysis is $5 \cdot 10^{-2}$ m^2/g. Prior to use the sand was washed in a pH = 4 HCl solution, rinsed, and again washed in pH = 10 NaOH solution. The sand was subsequently rinsed until a neutral pH was obtained and dried at 373° Kelvin.

4.2. Column experiment procedure

Quartz sand was packed into a 0.37 × 0.015 m cylindrical glass column (Omnifit) resulting in a porosity of 0.325, pore volume of $2.13 \cdot 10^{-2}$ L, and slurry density, a, of $5.5 \cdot 10^3$ g/L. Solutions were pumped through the column at a constant volumetric flow rate, q, of $2 \cdot 10^{-6}$ m^3/min by HPLC pumps (Jasco). An in-line pH probe (Endress Hauser) and ion chromatograph (Dionex) measured the pH and sodium concentration of the effluent. Experiment solutions were prepared with ultrapure, degassed water. Ionic strength and acidity were adjusted by the addition of NaCl and NaOH or HCl respectively. Solutions were stored in airtight HDPE vessels blanketed with N_2 gas and stirred continuously. Solutions were pumped through an in-line degasser (Jasco) prior to injection into the column. Before each experiment, the initial solution was pumped through the column for sufficient time to ensure that the surfaces were in chemical equilibrium with the flowing solution. This was achieved by monitoring the effluent and influent chemistry, until they were similar for 15 pore volumes. Further details on experimental techniques are provided in McNeece and Hesse (2016).

5. Discussion

Despite the apparent simplicity of acidity-salinity transport through quartz sand, it hasbeen proven challenging to accurately capture the observed coupling in reactive transport models. For example, the reference model defined in Section 2.1 predicts a stronger coupling in basic conditions than in acidic conditions, as is evident from the hodograph plane. In contrast, experimental results by McNeece and Hesse (2017) show that the magnitude of the coupling is comparable in both acidic and basic regimes. Most notably, any adjustment that improves the fit of the reference model under acidic conditions, leads to a deterioration of the fit in the basic regime, and vice versa. This implies that the model form, rather than parameterization, is responsible for the mismatch.

However, many surface chemistry model formulations have been proposed for the interaction of acidity and salinity within the quartz-water interface. Many of these models assume the basic structure of the triple layer model, but vary in the type of reactive sites, the number of reactions associated with each site, as well as whether co-ions form inner- or outer-sphere complexes. The hodograph plane is a useful tool to explore the role of model formulation in the acidity-salinity coupling.

The reference model considers only a single reactive site, with a single protonation reaction, and assumes that co-ions form outer-sphere complexes. In an attempt to capture the observed behavior, in the simplest expansion possible we include an additional proton uptake in the single site model, Eq. (3), which then requires outer-sphere surface complexation of the chloride ion, Eq. (5). Such a formulation for the quartz surface has been previously used to successfully model batch titration data (Duval et al., 2002). We refer to this model formulation as the "two-step model." We set the chloride binding constant equal to that of sodium to minimize the number of parameters $K_{Na} = K_{Cl} = 10^{-1.9}$, as is done by Hiemstra et al. (1989).

In the following analysis we consider the effect of the proton sorption reaction constants, $K_{H,1}$ and $K_{H,2}$, on the transport behavior, via the hodograph plane. To limit the number of adjustable parameters, we require that the point of zero charge (p.z.c.) is fixed at pH $= 3$ ($\mathbf{c}_H \approx 10^{-3}$ M) (Kosmulski, 2001). With this constraint, $K_{H,1}$ and $K_{H,2}$ are not independent, and we can think of the overall surface protonation reaction, combining reactions (2) and (3),

$$\equiv \mathrm{SiO^-} + 2\mathrm{H^+} \leftrightarrow \equiv \mathrm{SiOH_2^+}, \tag{31}$$

with the law of mass action being,

$$\hat{K} = \frac{[\equiv \mathrm{SiOH_2^+}]}{[\equiv \mathrm{SiO^-}]\{\mathrm{H^+}\}^2}. \tag{32}$$

At the p.z.c. the mineral surface is neutral. In the case that Na^+ and Cl^- sorption is negligible (Fig. 1), this implies that $[\equiv \mathrm{SiOH_2^+}] = [\equiv \mathrm{SiO^-}]$. By incorporating these assumptions into Eq. (32) one obtains

$$\hat{K} = K_{H,1}K_{H,2} = 10^6 \tag{33}$$

thus constraining the proton reaction constants relative to one another.

The surface charge as a function of pH is shown in Fig. 9 for a range of $K_{H,1}$ and $K_{H,2}$ values. As the strength of the first proton sorption reaction decreases, the charge of the quartz surface increases in magnitude. The increase in charge allows a greater dependence of the electrostatic behavior of the diffuse layer on salinity, see Eq. (10). As a result, the composition paths of the fast wave become more deflected in the acidic regime as $K_{H,1}$ decreases and $K_{H,2}$ increases. This trend is shown in Fig. 10 via the hodograph plane. Panel a shows a parameterization of the two-step model which produces similar behavior to the reference model. In this model the fast paths in the acidic regime are nearly vertical, hence, the predicted acidity-salinity coupling is weak.

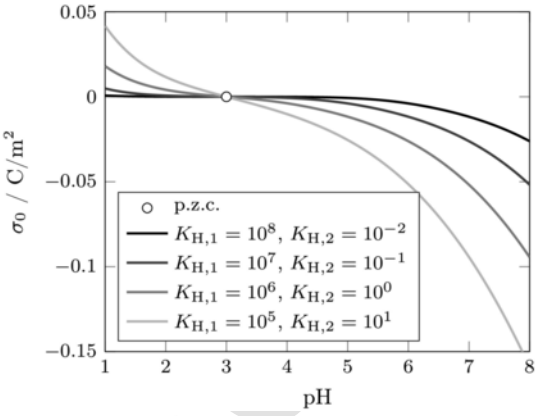

Fig. 9. P.Z.C. constraint. The evolution of the quartz surface charge as a function of pH for a range of parameter values, keeping a p.z.c. of 3.

In panels b–d, the relative importance of the second proton reaction increases, and the fast path is increasingly deflected, leading to a more symmetrical hodograph plane. Therefore, the acidity-salinity coupling increases with the strength of the second proton sorption reaction. Column experiments are plotted on the hodograph plane as a reference for the model predictions.

The elution history of each experiment is plotted in panels e–f of Fig. 10. With increasing $K_{H,2}$ we see an improved fit to the intermediate states of all experiments, particularly in the acidic regime (Fig. 10f,h). The intermediate state in the basic regime remains unchanged, though we see an increase in the second wave arrival time, relative to the experimental results. The disagreement in experiment 3 can presumably be explained through mixing, as the experimental results are smoothed. However, the model predictions of experiment 1 consistently show an unrealistically slow arrival time of the second wave. This implies the surface is less reactive in the basic regime than the model predicts.

Though the quartz surface has an overall negative charge in the pH range studied here, this does not exclude the secondary proton sorption reaction, which leads to local positive charge on the surface. The improved fit of the intermediate states, suggests that such a reaction is important for acidity-salinity coupling. Despite the low p.z.c., the secondary proton sorption reaction should not be dropped for quartz sand. In addition, the lack of agreement in the second wave arrival time suggests further improvement is necessary. An additional measure could include a second sorption site as suggested by Ong et al. (1992) and Leung et al. (2009).

6. Conclusion

Here we have extended the chromatographic analysis to geochemical surface complexation models and obtained the appropriate sorption isotherms that determine reactive transport behavior. Our analysis has shown that acidity-salinity coupling in reactive transport models can be understood in the context of chromatographic theory. This analysis provides a graphical representation of the overall transport behavior, and allows comparison under varying chemical conditions by inspection. Further, differing models can be compared directly, allowing a rapid analysis of the effect of model form on predicted transport behavior. Given that this analysis can be applied to any chemical system at local chemical equilibrium, it provides a powerful tool for reactive transport modeling, where model formulations and parameters abound.

Acknowledgments

This work was funded as part of the Center for Frontiers of Subsurface Energy Security, an Energy Frontier Research Center funded by

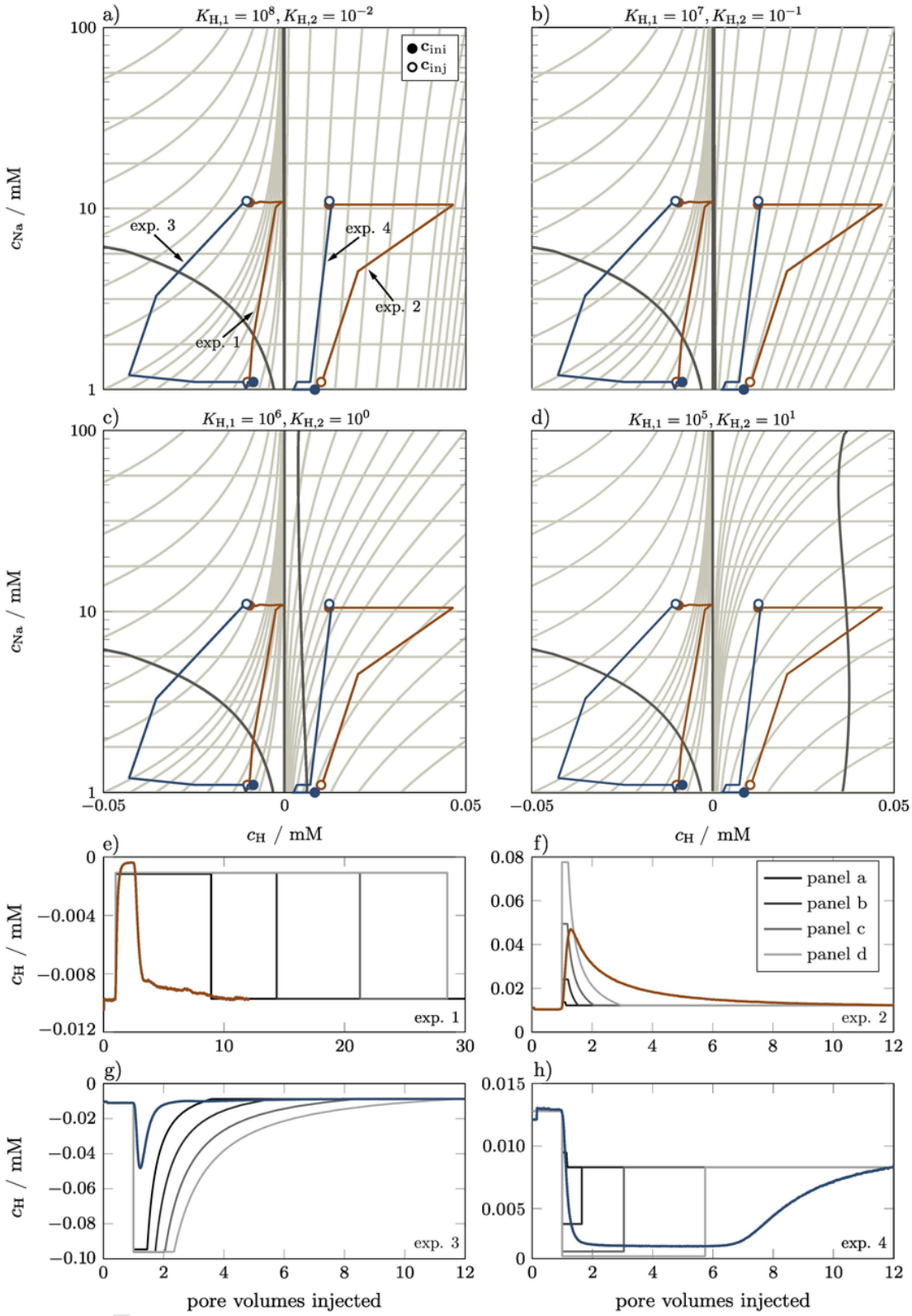

Fig. 10. Equilibrium constant variation. Column experiments are shown overlain on the hodograph plane of the two-step model with a) $K_{H,1} = 10^8$, $K_{H,2} = 10^{-2}$ b) $K_{H,1} = 10^7$, $K_{H,2} = 10^{-1}$ c) $K_{H,1} = 10^6$, $K_{H,2} = 10^0$ and d) $K_{H,1} = 10^5$, $K_{H,2} = 10^1$, where the colored lines are the experimental results. The elution curves of experiments e) 1, f) 2, g) 3, and h) 4 are compared against the model predicted results for each model parameterization.

the U.S. Department of Energy, Office of Science, Basic Energy Sciences under award #DE-SC0001114.

Appendix A. Hyperbolic theory

Consider again the hyperbolic limit of the transport equation (19). Dividing by the accumulation term yields

$$\mathbf{c}_\tau + \mathbf{f}(\mathbf{c})\mathbf{c}_z = 0. \tag{A.1}$$

In this form the conservation law now resembles the classic presentation of LeVeque (1992) where $\mathbf{f}(\mathbf{c}) = (\mathbf{I} + \nabla_c \mathbf{s}(\mathbf{c}))^{-1}$. A more appropriate similarity variable is then

$$\zeta := z/\tau, \tag{A.2}$$

such that characteristics now have constant velocity rather than retardation.

Again, substitution of η reduces the systems of partial differential equations to ordinary differential equations in the form of an eigenvalue problem

$$\left(\mathbf{f}(\mathbf{c}) - \lambda_p(\mathbf{c})\right)\mathbf{v}_p = 0, \tag{A.3}$$

where $\lambda_p(\mathbf{c}) = \zeta = z/\tau$ are the eigenvalues and

$$\mathbf{v}_p(\mathbf{c}) = \left(\frac{\mathrm{d}\mathbf{c}}{\mathrm{d}\zeta}\right)_p \tag{A.4}$$

are the eigenvectors.

References

Ahmed, S.M., 1966. Studies of the dissociation of oxide surfaces at the liquid-solid interface. Can. J. Chem. 44 (14), 1663–1670. https://doi.org/10.1139/v66-251.

Anderson, J., Wickersheim, K., 1964. Near infrared characterization of water and hydroxyl groups on silica surfaces. Surf. Sci. 2 (Supplement C), 252–260 http://www.sciencedirect.com/science/article/pii/0039602864900640https://doi.org/10.1016/0039-6028(64)90064-0, (ISSN 0039-6028).

Appelo, C.A.J., Postma, D., 2005. Geochemistry, Groundwater and Pollution. CRC Press.

Bolt, G.H., 1957. Determination of the charge density of silica sols. J. Phys. Chem. 61 (9), 1166–1169. https://doi.org/10.1021/j150555a007.

Charbeneau, R., 1981. Groundwater contaminant transport with adsorption and ion exchange chemistry: method of characteristics for the case without dispersion. Water Resour. Res. 17 (3), 705–713.

Charbeneau, R.J., 1988. Multicomponent exchange and subsurface solute transport: characteristics, coherence, and the Riemann problem. Water Resour. Res. 24 (1), 57–64.

Davies, C.W., 1962. Ion Association. Butterworths, Washington.

Duval, Y., Mielczarski, J.A., Pokrovsky, O.S., Mielczarski, E., Ehrhardt, J.J., 2002. Evidence of the existence of three types of species at the quartz-aqueous solution interface at ph 0–10: XPS surface group quantification and surface complexation modeling. J. Phys. Chem. B 106 (11), 2937–2945.

Hiemstra, T., De Wit, J., Van Riemsdijk, W., 1989. Multisite proton adsorption modeling at the solid/solution interface of (hydr)oxides: a new approach II. application to various important (hydr)oxides. J. Colloid Interface Sci. 133 (1), 105–117.

Johansen, T., Wang, Y., Orr, F.M., Dindoruk, B., 2005. Four-component gas/oil displacements in one dimension: part I: global triangular structure. Transp. Porous Media 61 (1), 59–76. https://doi.org/10.1007/s11242-004-6748-6, (ISSN 0169-3913).

Koretsky, C.M., Sverjensky, D.A., Salisbury, J.W., D'Aria, D.M., 1997. Detection of surface hydroxyl species on quartz, γ-alumina, and feldspars using diffuse reflectance infrared spectroscopy. Geochim. Cosmochim. Acta 61 (11), 2193–2210 http://www.sciencedirect.com/science/article/pii/S0016703797000562https://doi.org/10.1016/S0016-7037(97)00056-2, (ISSN 0016-7037).

Kosmulski, M., 2001. Chemical Properties of Material Surfaces. vol. 102, CRC Press.

Lake, L., 1989. Enhanced Oil Recovery, 1st edn. Prentice Hall.

Leung, K., Nielsen, I.M., Criscenti, L.J., 2009. Elucidating the bimodal acid- base behavior of the water- silica interface from first principles. J. Am. Chem. Soc. 131 (51), 18358–18365.

LeVeque, R., 1992. Numerical Methods for Conservation Laws. vol. 132, Springer.

Li, H., Bruyn, P.D., 1966. Electrokinetic and adsorption studies on quartz. Surf. Sci. 5 (2), 203–220 http://www.sciencedirect.com/science/article/pii/0039602866900823https://doi.org/10.1016/0039-6028(66)90082-3, (ISSN 0039-6028).

Lutzenkirchen, J., Marsac, R., Kulik, D.A., Payne, T.E., Xue, Z., Orsetti, S., Haderlein, S.B., 2015. Treatment of multi-dentate surface complexes and diffuse layer implementation in various speciation codes. Appl. Geochem. 55, 128–137 http://www.sciencedirect.com/science/article/pii/S0883292714001619https://doi.org/10.1016/j.apgeochem.2014.07.006, (ISSN 0883-2927, Geochemical Speciation Codes and Databases).

McNeece, C., Hesse, M., 2016. Reactive transport of aqueous protons in porous media. Adv. Water Resour. 97, 314–325 http://linkinghub.elsevier.com/retrieve/pii/S0309170816304729https://doi.org/10.1016/j.advwatres.2016.09.013, (ISSN 03091708).

McNeece, C.J., Hesse, M.A., 2017. Challenges in coupling acidity and salinity transport in porous media. Environ. Sci. Technol. 51 (20), 11799–11808. https://doi.org/10.1021/acs.est.7b02318, (PMID: 28876909).

Meeussen, J.C., Scheidegger, A., Hiemstra, T., van Riemsdijk, W.H., Borkovec, M., 1996. Predicting multicomponent adsorption and transport of fluoride at variable ph in a goethite-silica sand system. Environ. Sci. Technol. 30 (2), 481–488.

Meeussen, J.C.L., Kleikemper, J., Scheidegger, A.M., Borkovec, M., Paterson, E., van Riemsdijk, W.H., Sparks, D.L., 1999. Multicomponent transport of sulfate in a goethite-silica sand system at variable pH and ionic strength. Environ. Sci. Technol. 33 (19), 3443–3450. https://doi.org/10.1021/es981055s, (ISSN 0013-936X).

Morrow, B.A., Cody, I.A., 1976. Infrared studies of reactions on oxide surfaces. 5. Lewis acid sites on dehydroxylated silica. J. Phys. Chem. 80 (18), 1995–1998. https://doi.org/10.1021/j100559a009.

Ong, S., Zhao, X., Eisenthal, K.B., 1992. Polarization of water molecules at a charged interface: second harmonic studies of the silica/water interface. Chem. Phys. Lett. 191 (3–4), 327–335.

Pokrovsky, O., Golubev, S., Mielczarski, J., 2006. Kinetic evidences of the existence of positively charged species at the quartz-aqueous solution interface. J. Colloid Interface Sci. 296 (1), 189–194 http://www.sciencedirect.com/science/article/pii/S0021979705009355https://doi.org/10.1016/j.jcis.2005.09.001, (ISSN 0021-9797).

Prigiobbe, V., Hesse, M., Bryant, S., 2013. Hyperbolic theory for flow in permeable media with pH-dependent adsorption. SIAM J. Appl. Math. 73 (5), 1941–1957. https://doi.org/10.1137/130907185.

Prigiobbe, V., Hesse, M.A., Bryant, S.L., 2012. Anomalous reactive transport in the framework of the theory of chromatography. Transp. Porous Media 93 (1), 127–145. https://doi.org/10.1007/s11242-012-9947-6, (ISSN 0169-3913).

Rhee, H., Bodin, B., Amundson, N., 1971. A study of the shock layer in equilibrium exchange systems. Chem. Eng. Sci. 26, 1571–1580 http://www.sciencedirect.com/science/article/pii/0009250971860475.

Rhee, H.-K., Aris, R., Amundson, N., 2001. First-order Partial Differential Equations, Volume 1: Theory and Applications of Single Equations, Dover Books on Mathematics. ISBN: 978-0486419930.

Rhee, H.-K., Aris, R., Amundson, N.R., 1970. On the theory of multicomponent chromatography. Philos. Trans. R. Soc. A Math. Phys. Eng. Sci. 267 (1182), 419–455. https://doi.org/10.1098/rsta.1970.0050, (ISSN 1364-503X).

Rhee, H.-R., Aris, R., Amundson, N., 2001. First-order Partial Differential Equations, Volume 2: Theory and Applications of Hyperbolic Systems of Quasilinear Equations, Dover Books on Mathematics. ISBN: 978-0486419947.

Scheidegger, A., Borkovec, M., Sticher, H., 1993. Coating of silica sand with goethite: preparation and analytical identification. Geoderma 58 (1–2), 43–65 http://linkinghub.elsevier.com/retrieve/pii/001670619390084Xhttps://doi.org/10.1016/0016-7061(93)90084-X, (ISSN 00167061).

Scheidegger, A., Buergisser, C.S., Borkovec, M., Sticher, H., Meeussen, H., Riemsdijk, W.V., 1994. Convective transport of acids and bases in porous media. Water Resour. Res. 30 (11), 2937–2944.

Sposito, G., 2004. The Surface Chemistry of Natural Particles. Oxford University Press.

Sverjensky, D.A., 2005. Prediction of surface charge on oxides in salt solutions: revisions for 1:1 (M^+L^-) electrolytes. Geochim. Cosmochim. Acta 69 (2), 225–257 http://linkinghub.elsevier.com/retrieve/pii/S0016703704004557https://doi.org/10.1016/j.gca.2004.05.040, (ISSN 00167037).

Temple, B., 1983. Systems of conservation laws with coinciding shock and rarefaction curves. Contemp. Math. 17, 143–151.

Westall, J., Hohl, H., 1980. A comparison of electrostatic models for the oxide/solution interface. Adv. Colloid Interf. Sci. 12 (4), 265–294.

White, W., 2013. Geochemistry. Wiley-Blackwell. ISBN: 978-0-470-65667-9.

Zoback, M.D., 2012. Managing the seismic risk posed by wastewater disposal. Earth Mag.